Ultrasonics 99 (2019) 105975

Contents lists available at ScienceDirect

Ultrasonics

journal homepage: www.elsevier.com/locate/ultras

# Inversion algorithm for Lamb-wave-based depth characterization of acoustic emission sources in plate-like structures

Brennan Dubuc, Arvin Ebrahimkhanlou, Stylianos Livadiotis, Salvatore Salamone*

*Department of Civil, Architectural and Environmental Engineering, University of Texas at Austin, 301E E Dean Keeton St, Austin, TX 78712, USA*

ARTICLE INFO

*Keywords:*
Acoustic emission
Elastodynamics
Finite element method
Guided waves
Inverse problems
Lamb waves
Nondestructive evaluation
Structural health monitoring

ABSTRACT

An inversion algorithm (termed AEDep) is proposed for estimating the depth of acoustic emission (AE) sources in plate-like structural components. The work is motivated by the need for characterizing early-stage fatigue crack growth in such components. The algorithm achieves depth estimation by automatically extracting the depth-dependent amplitude ratio between the fundamental Lamb modes which comprise the AE signals. A finite element model is designed to study the frequency-dependent forward problem of Lamb wave motion due to a given source, from which the relation between source depth and amplitude ratio is established. Elastodynamic theory is used to validate the model in the frequency domain, as well as to derive a sensor tuning factor which may be incorporated into the solution. The proposed algorithm was tested on two plate-like specimens: a 6061-T6 aluminum plate and a 2025-T6 aluminum aircraft fuselage panel. Validation of the algorithm was achieved by generating controlled AE sources at various depths along the edges of the specimens, in the form of Hsu-Nielsen pencil lead breaks. Good agreement was found in the aluminum plate between the true and estimated source depths. A slight decrease in accuracy was found in the fuselage panel between the true values and their estimations. However, both experimental cases demonstrated the ability to distinguish between sources originating near the mid-plane of a plate-like structure from those near the surface. Lastly, the fast computation of the inversion algorithm shows strong potential for real-time monitoring applications.

## 1. Introduction

In nondestructive testing and structural health monitoring, there is a hierarchy of damage diagnosis [1]. Beyond lower-level diagnosis such as damage detection and localization, it is extremely valuable to perform damage characterization. For instance, determining the depth of an advancing fatigue crack through the thickness of a plate-like structure provides essential damage information during the early stage of crack propagation. Indeed, the stress intensity factor is a function of the crack depth (e.g. when originating from a hole [2]), with the range of the stress intensity factor governing the crack growth rate [3]. The early stage of crack propagation (beginning at the microstructural scale) is an important one, constituting more than 60% of a component's lifespan [4]. In the last decades, the acoustic emission (AE) method has advanced to perform damage detection and localization [5–8], as well as limited amounts of characterization [9–12]. The operating principle of AE involves monitoring acoustic energy emitted from damage evolution, and its success in these aspects arises from the sensitivity of the acoustic waves to various damage characteristics.

To monitor large plate-like structures, Lamb wave-based AE must be considered, in which the waveguide formed by the structure and its effect on wave propagation may be leveraged. In particular, a number of studies in the literature considered using Lamb wave properties to estimate the characteristics of AE sources. These included the source mechanism, risetime, and orientation (e.g. in-plane or out-of-plane mechanisms). For instance, Sato [13] studied the radiation pattern of the fundamental symmetric Lamb mode emitted from various simulated cracking mechanisms in metallic plates. On another note, Hamstad [14] suggested that the source risetime in a plate may be characterized by extracting modal information across frequency. As regards estimating source orientation, a variety of researchers have exploited the orientation-dependent nature of Lamb mode waveforms [15–21]. These included applications of sparse reconstruction [19], pattern recognition [20], and dynamic time warping [21].

Although various researchers considered estimating source orientation (via modal amplitudes in particular) [15–19], less attention has been paid to estimating source depth. However, it has recently been emphasized that an inversion algorithm is needed to convert modal characteristics to source depth [22,23]. To the best of the authors' knowledge, there have not been any efforts in the literature made for

* Corresponding author.
*E-mail address:* salamone@utexas.edu (S. Salamone).

https://doi.org/10.1016/j.ultras.2019.105975
Received 22 May 2019; Received in revised form 10 July 2019; Accepted 6 August 2019
Available online 08 August 2019
0041-624X/ 

source depth characterization in plate-like structures. Additionally, only limited work has been carried out on source characterization in realistic structural components, which may have geometric complexities (e.g. rivets, stringers, etc.). The performance of current approaches on realistic structures is therefore unclear.

This paper develops an inversion algorithm capable of extracting and converting modal amplitudes to AE source depth. The main idea is that the amplitude ratio between the fundamental antisymmetric and symmetric Lamb modes serves as a dimensionless quantity related to source depth. The algorithm first uses recorded AE signals and an estimated planar source location to generate trial signals with various amplitude ratios. Afterward, it uses a correlation-based metric to extract the amplitude ratio from the recorded signals. The conversion from amplitude ratio to source depth is then made using knowledge about the given source type. In this case, the forward problem is solved using finite element method (FEM) modeling, which establishes the frequency-dependent relation between amplitude ratio and source depth. The algorithm is evaluated by experimentally simulating controlled AE sources at various depths along the edges of two plate-like specimens. First, benchmark testing is conducted on an aluminum plate specimen. Afterward, to evaluate performance on a realistic structure, the algorithm is tested on a plate-like section of an aircraft fuselage. The primary assumptions underlying the experiments are: (1) the plate-like structures are composed of an isotropic elastic material; and (2) the pencil lead breaks may be considered as point force excitations.

This paper is organized as follows: First, an elastodynamic theory for Lamb wave motion due to buried point forces is presented in Section 2, from which the FEM model is designed and validated. Subsequently, the model is used to study edge point forces (representative of controlled AE sources) beyond the limits of the theory. The inversion algorithm is then presented in Section 3. The experiments used to validate the algorithm under controlled AE sources are detailed in Section 4, with the results presented and discussed in Section 5. Afterward, conclusions and recommendations for future work are made in Section 6.

## 2. Forward problem: wave motion due to point forces

This section details Lamb wave motion on the surface of a plate due to buried and edge horizontal point forces. A theoretical analysis is first overviewed for a buried force, while incorporating sensor tuning effects. A FEM model is then described and validated for a buried force. After validation, the model is used to study edge forces, for which only approximate theoretical formulations are available [24]. For each case, the use of the amplitude ratio between the fundamental Lamb modes as a means of inferring source depth is outlined.

### 2.1. Elastodynamic theory for buried force excitation

Elastodynamic theory has been developed to describe the excitation of Lamb modes due to a buried horizontal point force in an infinite isotropic elastic plate [25], as illustrated in Fig. 1(a). Without loss of generality, let a unit horizontal point force $F$ be located in cylindrical coordinates at $(r, \theta, z) = (0, 0, z')$ and directed along $\theta = 0$. Further, let the mid-plane of the plate be $z = 0$, with the top and bottom surfaces located at $z = \pm h$. A harmonic source with angular frequency $\omega$ is considered, so that the force is $F = e^{-i\omega t}$. Additionally, let an arbitrary sensor (say, sensor 0) be located on the plate surface with coordinates $(r_0, \theta_0, h)$ as shown in Fig. 1(a).

It is assumed that the sensor only records the scalar $z$ component of displacement on the top surface of the plate [26]. The displacement $u_0$ of a given Lamb mode due to such a force can be expressed in cylindrical coordinates as [25]

$$u_0 = A\cos(\theta_0)H_1^{(1)}(kr_0)e^{-i\omega t} \tag{1}$$

where $A$ is the amplitude of the mode (see Appendix A), and $k$ is the frequency-dependent wavenumber of the mode (determined from the Rayleigh-Lamb dispersion equations [27]). The Hankel function $H_1^{(1)}(\cdot)$ incorporates spatial phase propagation and geometric attenuation due to the resulting circular-crested wavefront. For simplicity, the Hankel function may be approximated by its far-field asymptote $H_1^{(1)}(\kappa) \approx -\sqrt{2i/\pi\kappa}e^{i\kappa}$ [28], with the asymptote being reached roughly 3 wavelengths from the source [27]. The far-field displacement is then

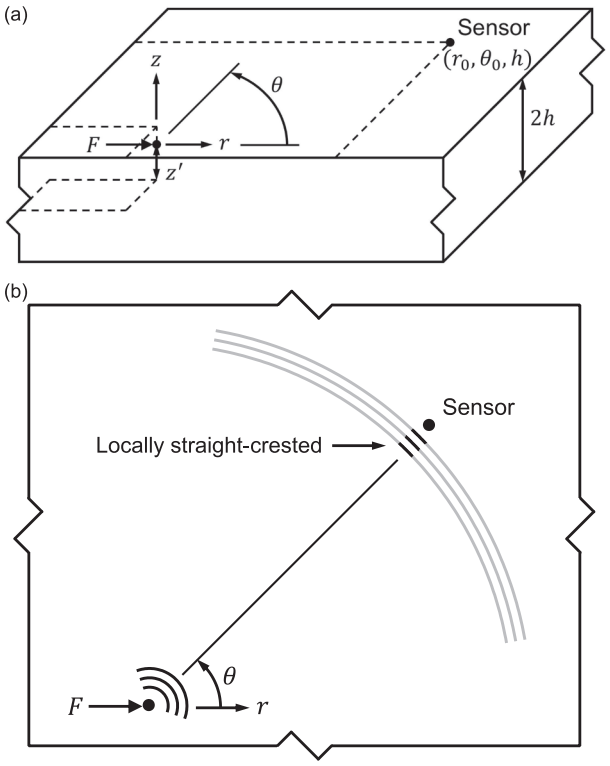


**Fig. 1.** (a) Schematic of buried force excitation in plate and sensor location on surface. (b) Top-view illustration of circular-crested wavefronts due to point force excitation as approximately straight over small sensor area. Note: plate extends to infinity in $(r, \theta)$ plane.

$$u_0 = -\sqrt{\frac{2i}{\pi k r_0}}A\cos(\theta_0)e^{i(kr_0-\omega t)} \tag{2}$$

A circular sensor of diameter $D$ is considered to record the surface displacement $u_0$. For wavelengths on the order of the sensor diameter, the effects of the finite sensor size must be incorporated. To this aim, it is assumed that the sensor records an average displacement over its cross-sectional area [29]. To aid in the calculation, it is also assumed that the circular-crested wavefronts are locally straight in the far-field over the small area of a sensor, as depicted in Fig. 1(b). The circular sensor is then approximated by a rectangle with effective dimensions $b \times D$, as illustrated in Fig. 2. As shown in the figure, the effective sensor size $b$ which a straight-crested wave interacts with is obtained from the following average:

$$b = \frac{1}{D}\int_{-\pi/2}^{\pi/2}\left[D\cos(\phi)\right]\left[\frac{1}{2}D\cos(\phi)\mathrm{d}\phi\right] = \frac{\pi D}{4} \tag{3}$$

Moreover, for a sensor centered at $r_0 = nD$ from the source, the $1/\sqrt{r_0}$ attenuation from Eq. (2) produces a proportional amplitude difference of

$$\frac{\left(nD - \frac{1}{2}D\right)^{-1/2} - \left(nD + \frac{1}{2}D\right)^{-1/2}}{\left(nD - \frac{1}{2}D\right)^{-1/2}} = 1 - \sqrt{\frac{2n-1}{2n+1}} \tag{4}$$

across its diameter. This difference is less than 5% at only $n = 10$

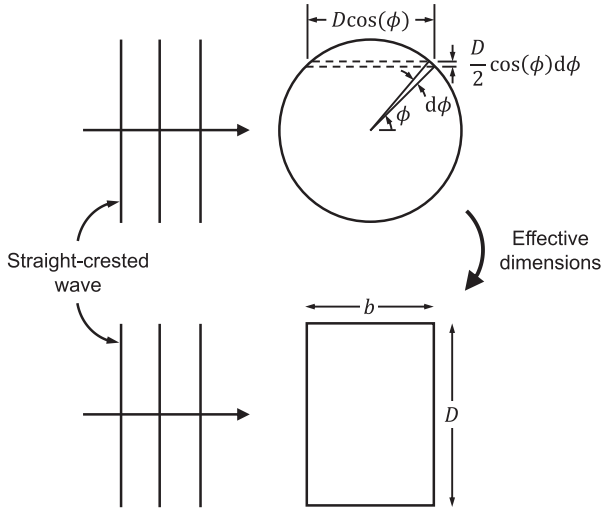


**Fig. 2.** Top-view schematic of straight-crested wave interacting with circular sensor of diameter $D$, and effective rectangular sensor achieving equivalent average displacement over the cross-section. Arbitrary differential segment used to obtain the effective size $b$ is shown by dashed line.

diameters from the source. Therefore, the wavefronts are also assumed to be locally non-attenuative over the sensor diameter. From these considerations, the average displacement which the sensor records is

$$U_0 = -\sqrt{\frac{2\mathrm{i}}{\pi k r_0}} A\cos(\theta_0)\frac{1}{b}\int_{-b/2}^{b/2} e^{\mathrm{i}(k\rho-\omega t)}\mathrm{d}\rho$$
$$= -\sqrt{\frac{2\mathrm{i}}{\pi k r_0}} A\mathrm{sinc}\left(kb/2\right)\cos(\theta_0)e^{-\mathrm{i}\omega t} \tag{5}$$

where . The sinc(·) factor accounts for how well the sensor size is tuned to a given mode's wavelength. It may be noted that the same tuning factor is also found for excitation (as opposed to reception) of straight-crested waves from a rectangular sensor of size $b$[30].

With the mode amplitude $A$ a function of the source depth $z'$[25], the depth may be inferred by measuring the amplitude. However, since absolute measurements of amplitude require sensor calibration [26], relative amplitude measurements may be more practical. Inspired by earlier work on classifying AE sources [19], the amplitude ratio between the $A_0$ and $S_0$ modes is used here as a dimensionless quantity to infer the source depth. From Eq. (5), the amplitude ratio may be expressed

$$R = \frac{U_{0,\mathrm{a}}}{U_{0,\mathrm{s}}} = \sqrt{\frac{k_\mathrm{s}}{k_\mathrm{a}}}\frac{\mathrm{sinc}(k_\mathrm{a}b/2)}{\mathrm{sinc}(k_\mathrm{s}b/2)}\frac{A_\mathrm{a}}{A_\mathrm{s}} \tag{6}$$

where subscripts a and s denote $A_0$ and $S_0$, respectively. It may be seen that the amplitude ratio is independent of the $(r_0, \theta_0)$ sensor coordinates. The same amplitude ratio may therefore apply to any sensor location (within the far-field).

### 2.2. FEM model for buried and edge force excitation

As opposed to buried forces in the interior of a plate, it is only feasible to experimentally generate horizontal point forces on the edge of a plate. Furthermore, since only approximate theories have been developed for an edge force [24], it is studied here numerically using FEM modeling. To this aim, a 2D plane-strain model is designed, with the 3D solution obtained during post-processing.

The 2D FEM model is designed in Abaqus for straight-crested Lamb wave motion due to a line force excitation, as illustrated in Fig. 3(a) and (b) for buried and edge forces, respectively. For each case, the excitation is modeled in a 3.18-mm-thick plate, which extends 3 m from the excitation point. In order to study the behavior of various narrowband frequency regions and make comparisons to the frequency-domain results from the elastodynamic theory, a nearly harmonic excitation is adopted in the FEM modeling. Specifically, the time dependence of the force is set to a 30-cycle Hanning-windowed toneburst (1 N/m amplitude), and the center frequency is chosen between 300 and 500 kHz (0.95–1.6 MHz-mm). A structured mesh is created from four-node bilinear plane-strain quadrilaterial elements (CPE4R), which are roughly 1/15-th of the smallest wavelength considered (5.2 mm for $A_0$ at 500 kHz), or 0.4 mm × 0.4 mm. To avoid reflections, the $z$ component of displacement is measured 1 m from the force on each surface of the plate. The displacements of the $A_0$ and $S_0$ modes are then separated using their respective symmetry and antisymmetry over the cross-section [31]. Specifically, the displacements are added to isolate $A_0$ and subtracted to isolate $S_0$.

For a Hanning-windowed toneburst with center frequency $f_\mathrm{c}$, the displacement for a given mode recorded at $r = 1$ m from the force has the following wavepacket form:

$$u_\mathrm{fem} = A_\mathrm{fem} H(t) e^{\mathrm{i}(k-\omega_\mathrm{c} t)} \tag{7}$$

where $A_\mathrm{fem}$ is the amplitude of the mode, $H(t)$ denotes the time dependence of the wavepacket's envelope, $\omega_\mathrm{c} = 2\pi f_\mathrm{c}$ is the angular frequency, and $k$ is the wavenumber of the mode at $\omega_\mathrm{c}$. It has been found that the Lamb mode amplitude due to a point force excitation is related to the amplitude due to a corresponding line force as [31]

$$A_\mathrm{point} = \frac{\mathrm{i}k}{2} A_\mathrm{line} \tag{8}$$

Therefore, the amplitude ratio for a point force (i.e. the 3D solution) may be obtained from the 2D FEM line force amplitudes as

$$R_\mathrm{fem} = \sqrt{\frac{k_\mathrm{a}}{k_\mathrm{s}}}\frac{\mathrm{sinc}(k_\mathrm{a}b/2)A_\mathrm{a,fem}}{\mathrm{sinc}(k_\mathrm{s}b/2)A_\mathrm{s,fem}} \tag{9}$$

where the amplitude decay and sensor tuning factors from Eq. (5) are also included.

In order to validate the FEM model, the results are first compared to the elastodynamic theory for a buried force in an aluminum plate, as shown in Fig. 4. This corresponds to the FEM model in Fig. 3(a), along with the theoretical amplitude ratio from Eq. (6). The required material properties for modeling aluminum are listed in Table 1[32]. Results are shown for quarter- and top-plane source depths, $z' = h/2$ and $h$, respectively, with ten FEM runs show for each case at various frequencies. The trivial case of mid-plane excitation ($z' = 0$) is not shown, since the problem is purely symmetric and hence the amplitude ratio is identically zero. For simplicity, the sensor is taken as a point sensor (i.e. $D = b = 0$), so that the sensor tuning factor has no effect. The predictions of the FEM model show good agreement with the theoretical solution for a buried force, indicating that the model may be generalized to study edge forces as well.

Amplitude ratio predictions using the FEM model in Fig. 3(b) for an edge force excitation in an aluminum plate are shown in Fig. 5. Like Fig. 4, the results are shown for a point sensor. To investigate the depth dependence of the amplitude ratio, three sets of FEM predictions (ten runs in each) are shown over a range of source depth. Only the top-half of the plate thickness is shown, since the amplitude ratio is symmetric with respect to the mid-plane of the plate [25]. The amplitude ratio is monotonic over one half of the plate thickness, yielding the potential for source depth characterization from the mid-plane to the surface. As such, a function may be created which maps amplitude ratio to source depth at a given center frequency. To this aim, a second-order polynomial function may be fit to the FEM prediction, as shown in Fig. 5. Since the amplitude ratio is known to be zero at the origin [25], the polynomial fit is forced to satisfy $R_\mathrm{fem} = 0$ at $z' = 0$,

$$R_\mathrm{fem} = p\frac{z'}{h} + q\left(\frac{z'}{h}\right)^2 \tag{10}$$

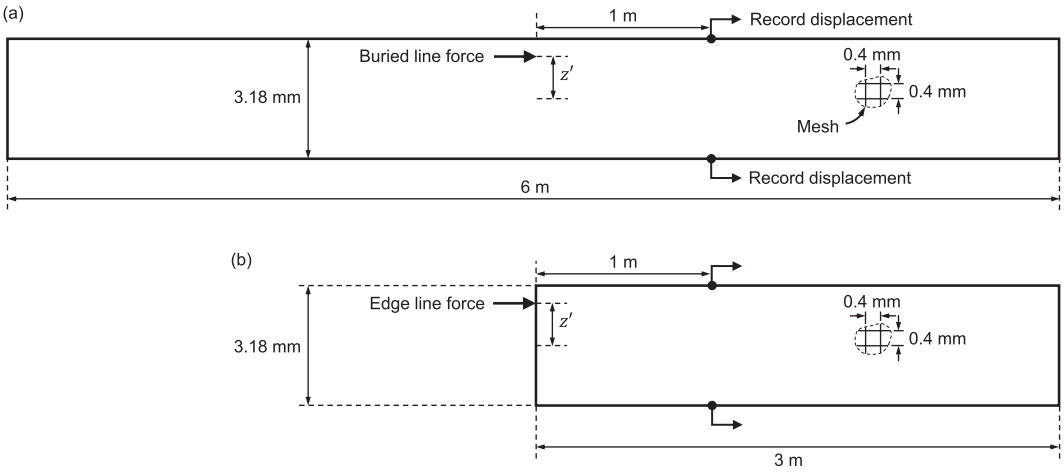


**Fig. 3.** Schematic of 2D FEM model for (a) buried and (b) edge line force excitation in an aluminum plate (not drawn to scale).

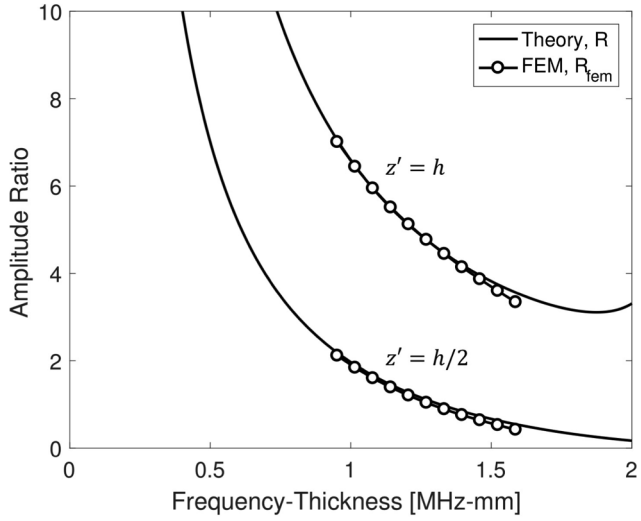


**Fig. 4.** Validation of FEM model for buried force excitation in aluminum plate for different source depths $z'$, as recorded by point sensor.

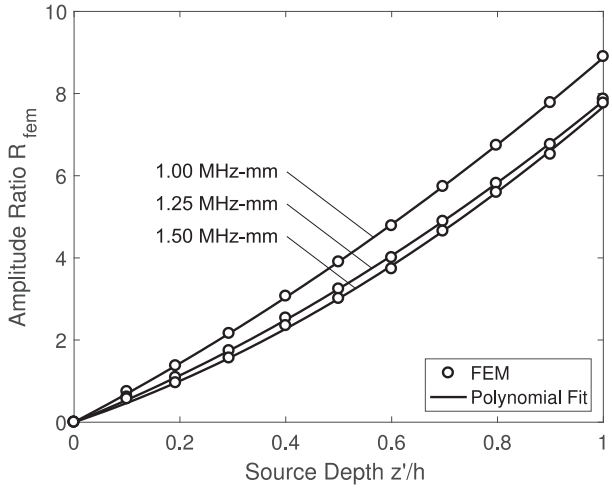


**Fig. 5.** FEM predictions for amplitude ratio due to edge force excitation in aluminum plate at various frequency-thicknesses, as recorded by point sensor. Second-order polynomial fit overlain for each.

**Table 1**
Material properties for 6061-T6 aluminum: density $\rho$, Lamé constants $\lambda$, $\mu$.

| Property | Value |
|---|---|
| $\rho$ | 2700 kg/m$^3$ |
| $\lambda$ | 54.3 GPa |
| $\mu$ | 27.2 GPa |

**Table 2**
FEM polynomial fitting parameters $p, q$ for amplitude ratio at various frequency-thicknesses [MHz-mm], as recorded by point sensor.

| Frequency-thickness | $p$ | $q$ |
|---|---|---|
| 1.00 | 6.75 | 2.13 |
| 1.25 | 5.16 | 2.66 |
| 1.50 | 4.36 | 3.32 |

where the fitted parameters $p$, $q$ are functions of frequency-thickness. Values of these parameters are collected in Table 2 for various cases.

## 3. Inverse problem: inversion algorithm

Source depth estimation is performed as shown in the flowchart of Fig. 6. The flowchart details the inversion algorithm (termed AEDep) for automatically extracting the amplitude ratio from $N$ AE signals and converting it to source depth. The algorithm is composed of an initialization stage and a depth estimation stage, as described below.

### 3.1. Initialization stage

To perform depth estimation, the source must first be localized in the plane of the plate-like structure. The AEDep algorithm is made sufficiently general so that any user-preferred method may be used for this initialization step, such as triangulation [33], touch and learn [34], or sparse reconstruction [35]. For simplicity, as well as to examine the performance of source depth estimation in a typical scenario, a traditional triangulation method is implemented here, as described in Appendix B. The resulting 2D source location in cartesian coordinates is denoted $\mathbf{x}^\star = [x^\star\ y^\star]^T$, where a superscript $T$ indicates transpose.

Although a real excitation typically has a wideband source function [36,37], bandpass filtering may be used to achieve narrowband conditions in experimental signals, thus simplifying their analysis [19,35]. To approximate the harmonic waveforms modeled in Section 2, a specific frequency is targeted by processing the signals $s_1, \ldots, s_N$ (recorded by $N$ sensors) through a narrowband filter. To isolate the fundamental $A_0$ and $S_0$ modes, the center frequency $f_c$ is chosen below the first cutoff frequency (roughly 1.6 MHz-mm for an aluminum plate, as determined

from dispersion curves). For simplicity, the notation $s_1, \ldots, s_N$ is used from here onward to denote the filtered signals.

### 3.2. Depth estimation stage

Within the AEDep flowchart, information from the initialization stage is input to an amplitude ratio extraction step, from which the source depth is estimated. This is the main component of the inversion algorithm. The amplitude ratio extraction step is based on determining the maximum correlation between the AE signals and a set of trial signals (with known amplitude ratios). Let the concatenated AE signal from $N$ sensors be denoted $\mathbf{s} = [s_1^T \cdots s_N^T]^T$. Further, let the trial concatenated signals (determined below) be $\mathbf{S}_1, \ldots, \mathbf{S}_J$, where each $\mathbf{S}_j$ has a unique amplitude ratio $R_j$. Since only the amplitude information within the signals is relevant, the overbar notations $\bar{\mathbf{s}}$ and $\bar{\mathbf{S}}_j$ are used to denote the envelopes of the recorded and trial signals, respectively. For an arbitrary signal $s$, the envelope may be obtained using the Hilbert transform $\mathcal{H}\{\cdot\}$ as

$$\bar{s} = |s + i\mathcal{H}\{s\}| \tag{11}$$

where $|\cdot|$ denotes absolute value. Given a set of trial signals indexed by $j$, the index $j^\star$ achieving the maximum correlation is determined by using the inner product $\langle \cdot, \cdot \rangle$ as a correlation metric,

$$j^\star = \text{argmax}_j \langle \bar{\mathbf{s}}, \bar{\mathbf{S}}_j \rangle \tag{12}$$

To ensure there is no bias associated with the norm of individual trial signals, each is taken to satisfy $\|\bar{\mathbf{S}}_j\|_2 = 1$, where $\|\cdot\|_2$ denotes the $\ell_2$-norm. The extracted amplitude ratio is then

$$R^\star = R_{j^\star} \tag{13}$$

thus automating the amplitude ratio extraction.

With the amplitude ratio determined, it may be converted to source depth using an appropriate model. Since this paper considers characterizing edge forces, the FEM model presented in Section 2.2 is used for this purpose. In particular, the fitted polynomial in Eq. (10) is used to estimate the source depth given an extracted amplitude ratio $R^\star$,

$$\frac{z^\star}{h} = \sqrt{\frac{p^2}{4q^2} + \frac{R^\star}{q}} - \frac{p}{2q} \tag{14}$$

where the parameters $p$ and $q$ are those associated with the given sensor diameter $D$ and center frequency $f_c$. Since estimated depth values which exceed the plate thickness are not meaningful, any cases in which $z^\star/h > 1$ are set to 1.

#### 3.2.1. Trial signal creation

In this paper, a model-based approach is used to create the trial signals, as outlined in Fig. 6. This involves analytically propagating narrowband source spectra with various amplitude ratios from the estimated source location $\mathbf{x}^\star$ to the sensor locations $\mathbf{x}_1, \ldots, \mathbf{x}_N$. However, since the source spectra are not known *a priori*, they are estimated here using information from the measured signals. This is accomplished by isolating a propagated waveform within one of the signals and then backward propagating it to the source location.

To estimate the source spectrum, the first arrival mode wavepacket $U_1$ within the first sensor's signal is identified, as pictured in Fig. 7. For this purpose, let the sensor indices be chosen in order of ascending arrival time, such that the first sensor corresponds to the shortest arrival time. Although any sensor may be selected here, the first is chosen in order to maximize the signal-to-noise ratio. To further reduce noise artifacts, the wavepacket is fitted by a Gaussian modulated wavepacket with center frequency $f_c = \omega_c/2\pi$,

$$U_1(t) \approx G(t)e^{-i\omega_c t} \tag{15}$$

where $G$ is the Gaussian envelope (see Fig. 7), with mean and variance denoted $t_p$ and $\sigma$, respectively. Since only the amplitude is of interest,

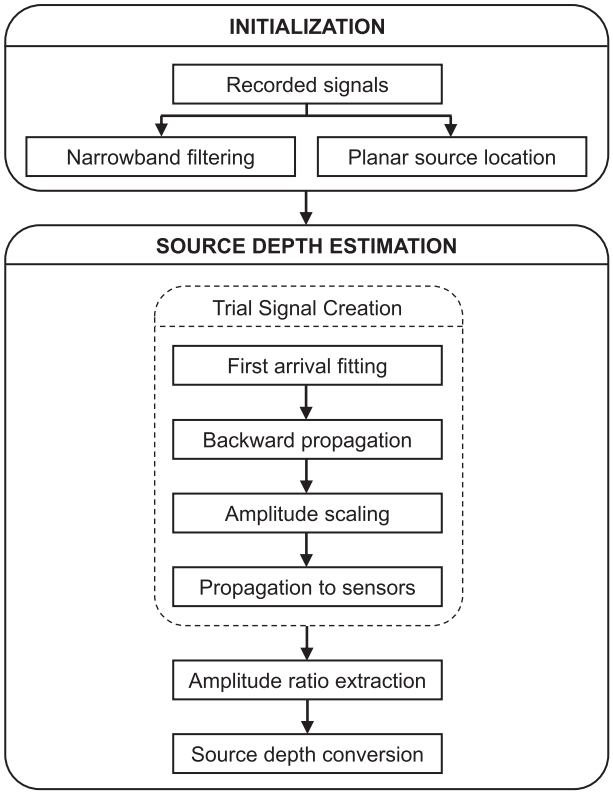


**Fig. 6.** Flowchart of inversion algorithm (AEDep) for AE source depth characterization.

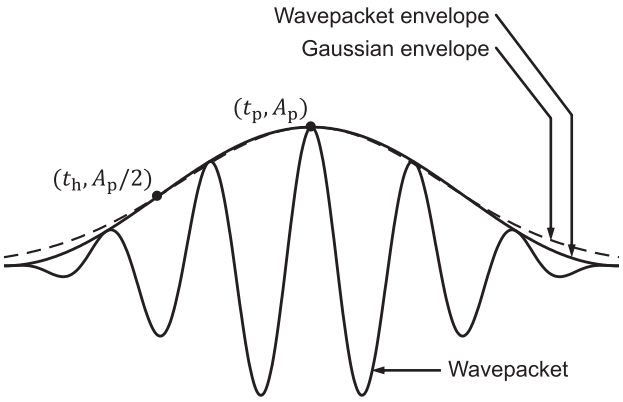


**Fig. 7.** Illustration for fitting of Gaussian envelope $G$ to the envelope of the first arrival wavepacket $U_1$. Two points used for fitting indicated by dots.

there is no need to match the phase in the Gaussian wavepacket to that in $U_1$. The fitting is then completed by measuring two unique points on the envelope of $U_1$. These are voluntarily taken as the peak $A_p$ and half-peak $A_p/2$, occurring at $t_p$ and $t_h$, respectively, as visualized in Fig. 7. With $(t_h, A_p/2)$ and $(t_p, A_p)$ serving as two known points on the Gaussian, the variance may be found as $\sigma^2 = (t_p - t_h)^2/2\ln(2)$, where $\ln(\cdot)$ denotes the natural logarithm. The first arrival spectrum $\widehat{U}_1$ may then be approximated by the spectrum of the Gaussian wavepacket, denoted $\widehat{G}$. With $G$ being Gaussian, this may be found explicitly as [19]

$$\widehat{G} = \sqrt{2\pi\sigma^2}A_p e^{i(\omega-\omega_c)t_p - (\omega-\omega_c)^2\sigma^2/2} \tag{16}$$

The source spectrum $\widehat{U}^\star$ may then be estimated by backward propagating the first arrival spectrum (as approximated through $\widehat{G}$). From Eq. (2), this may be written

$$\widehat{U}^\star = \sqrt{k_s}\widehat{G}e^{-ik_s r_1} \tag{17}$$

where $k_s$ is the wavenumber of the first arrival mode (i.e. $S_0$ for the considered frequency range), and $r_1 = ||\mathbf{x}^\star - \mathbf{x}_1||_2$ is the distance from the estimated source $\mathbf{x}^\star$ to sensor 1. Since the $\cos(\theta_0)$ and $-\sqrt{2i/\pi r_0}$ terms in Eq. (2) do not affect the final amplitude ratio, those terms are not included in the above backward propagation. The frequency spectrum $\widehat{U}_{j,n,m}$ of mode $m$ at sensor $n$, for a given amplitude ratio $R_j$, may then be obtained by scaling and propagating the source spectrum to that sensor,

$$\widehat{U}_{j,n,m} = \frac{A_{j,m}}{\sqrt{k_m}} \widehat{U}^\star e^{ik_m r_n} \tag{18}$$

where $m = \{a, s\}$ denotes $A_0$ and $S_0$, respectively, $A_{j,m}$ is the amplitude for mode $m$ given the trial ratio $R_j$, $k_m$ is the wavenumber for mode $m$, and $r_n$ is the distance from the estimated source to sensor $n$. Since the measured response implicitly contains the sensor tuning factor, the trial amplitudes $A_{j,m}$ are related to the ratio $R_j$ as

$$R_j = \sqrt{\frac{k_s}{k_a}} \frac{A_{j,a}}{A_{j,s}} \tag{19}$$

By voluntarily setting the $S_0$ amplitude to unity (i.e. $A_{j,s} = 1$), the $A_0$ amplitude is then determined from the amplitude ratio, $A_{j,a} = \sqrt{k_a/k_s} R_j$. The trial signal at sensor $n$ with amplitude ratio $R_j$ is found by superposing the two modes and transforming to the time domain as

$$S_{j,n} = \mathcal{F}^{-1}\left\{ \sum_m \widehat{U}_{j,n,m} \right\} \tag{20}$$

where $\mathcal{F}^{-1}\{\cdot\}$ denotes the inverse Fourier transform. The trial concatenated signal for a source with amplitude ratio $R_j$ is then formed as

$$\mathbf{S}_j = [S_{j,1}^T \cdots S_{j,N}^T]^T \tag{21}$$

It should be noted that the model defined through Eq. (20) only considers the first arrivals at each sensor. The inversion algorithm therefore extracts the amplitude ratio best describing the first arrivals in the measured signals. In this way, no knowledge of the boundaries of the plate-like structure are necessary.

## 4. Experiment

### 4.1. Aluminum plate

The inversion algorithm AEDep was first tested on a square $2h = 3.18$ mm (0.125 in.) thick 6061-T6 aluminum plate of length $L = 0.914$ m (3 ft). A schematic of the experiment may be seen in Fig. 8. The surface of the plate was instrumented (using hot glue) with $N = 4$ Physical Acoustics Corp. (PAC) PICO sensors, denoted $P_1$,...,$P_4$. The sensor diameter was $D = 4.78$ mm (0.188 in.), which yielded an effective sensor size of $b = 3.75$ mm (0.148 in.) from Eq. (3). The peak response of the sensors was near 470 kHz.

Acoustic emission due to horizontal edge forces was obtained using Hsu-Nielsen pencil lead breaks (PLBs) at 16 locations along the plate edge, as seen in Fig. 8. The PLBs (with 0.5 mm lead) were considered to be equivalent to point forces [38]. Due to the symmetry of the plate and the sensor locations, PLBs were only carried out within the lower righthand quarter of the plate. For each location, PLBs were performed at three source depths: mid-plane ($z' = 0$), quarter-plane ($z' = h/2$), and top-plane ($z' = h$). Since the amplitude ratio is symmetric with respect to the mid-plane [25], AE was only simulated over one half of the plate thickness. For each depth, the PLB was performed twice, resulting in 32 PLBs for each.

Recorded AE signals were preamplified at 40 dB (PAC 2/4/6 preamplifiers), sampled at 5 MHz, and stored on a Mistras Micro-Express data acquisition system (DAQ). The DAQ also had an on-board bandpass analog filter, with the cutoff frequencies set to 100 kHz and 1 MHz. The recorded signals were then post-processed through the inversion algorithm using a PC. The algorithm was implemented with $J = 100$ trial amplitude ratios. The range of trial ratios was taken between 0.1 and 10, yielding $(R_1, R_2, ..., R_J) = (0.1, 0.2, ..., 10)$. The recorded signals were then further bandpass filtered during post-processing using a fourth-order Butterworth filter. The center frequency $f_c$ was selected as the sensor's peak response at 470 kHz, with cutoff frequencies set at 445 and 495 kHz.

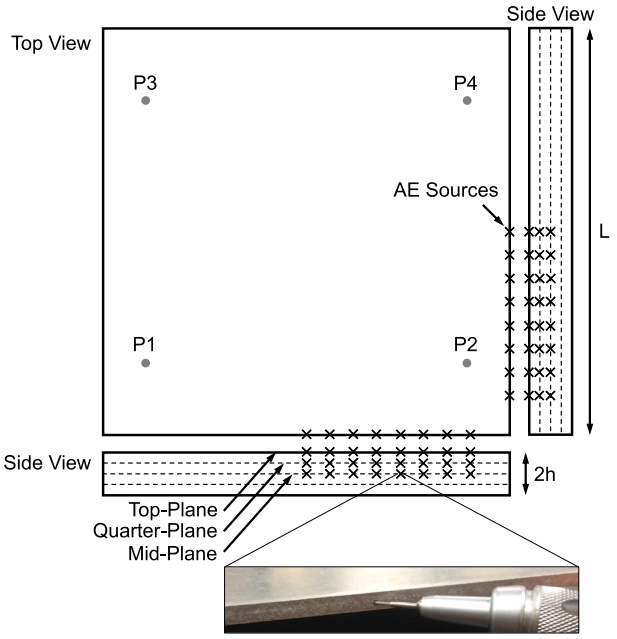


**Fig. 8.** Schematic of experimental setup and data acquisition for recording simulated acoustic emission in a square aluminum plate ($L = 0.914$ m, $2h = 3.18$ mm). Pencil lead break acoustic emission source locations indicated by crosses, with four sensors indicated as $P_1$,...,$P_4$.

### 4.2. Fuselage panel

To investigate the performance of the inversion algorithm on a more realistic structure, analogous experiments were also conducted on a 1.3 m × 1.1 m (50 in. × 44 in.) fuselage panel (2025-T6 aluminum) from a civilian aircraft, as shown in Fig. 9. It may be seen that the fuselage was composed of rounded rectangular segments which were locally homogeneous, at 2.0 mm (0.079 in.) in thickness, spanning an area of roughly 45 cm × 15 cm (18 in. × 6 in.). Near the riveted areas, the thickness of the fuselage panel roughly doubled, as indicated by the rounded lines in Fig. 9. Four PICO sensors were installed on the back side of the fuselage panel, and arranged semi-randomly. The goal of the sensor arrangement was to investigate the performance of the inversion algorithm with only two sensors installed per segment. For simplicity, only the lower right segments were instrumented.

Like the test on the aluminum plate, AE with different source depth was generated at various locations along the edge of the fuselage panel. Due to the smaller size of the investigated segments, only five locations were tested. Moreover, due to the smaller thickness of the fuselage, only two planes (top- and mid-plane) could be reliably used to tested. The recorded signals were preamplified, sampled, and filtered under the same conditions used in the aluminum plate. In addition, the trial amplitude ratios for the inversion algorithm were also the same.

## 5. Localization and depth estimation results

This section presents the experimental results obtained for the aluminum plate and fuselage panel. Results are discussed for planar localization using the triangulation technique, as well as source depth

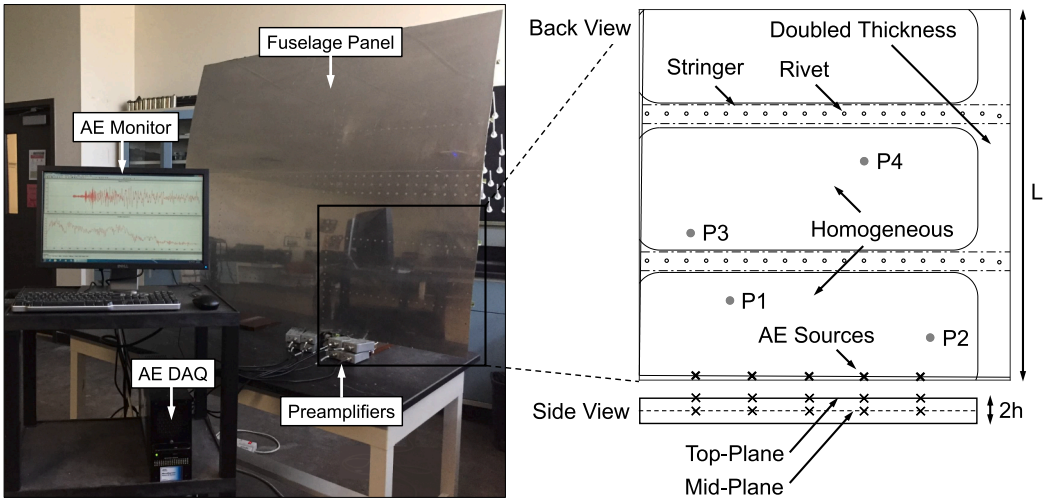


**Fig. 9.** Schematic of experimental setup and data acquisition for recording controlled acoustic emission sources in fuselage panel ($L = 0.50$ m, $2h = 2.0$ mm). Source locations indicated by crosses, with four sensors denoted $P_1$,…,$P_4$.

characterization using the inversion algorithm.

### 5.1. Aluminum plate

The results of planar localization using the iterative triangulation technique may be seen in Fig. 10(a)–(c) for the top-, quarter-, and mid-plane source depths, respectively. The results show good agreement with the true locations, with an average error of less than 1 cm (roughly 1% of plate length). It may be seen that the localization accuracy decreased slightly as the sources approached the plate corner. This may be due to reflections within the corner, poor location with respect to the sensors, or boundary conditions from the corner supports of the plate, for instance. Although the accuracy decreased in these cases, the absolute error never exceeded 2 cm.

In order to illustrate the recorded and trial signals, an example is shown in Fig. 11 for the concatenated recorded signal $\mathbf{s}$ from a randomly selected AE location ($x = 55$ cm, $y = 0$ cm) along the top-plane of the aluminum plate. Overlain is the concatenated trial signal $\mathbf{S}_{j^\star}$ whose amplitude ratio ($R^\star = 3.6$) achieved the greatest correlation with the recorded signal. Only the signal envelopes $\bar{\mathbf{s}}$ and $\bar{\mathbf{S}}_{j^\star}$ are shown, with dashed lines distinguishing the signals from each of the four sensors. It may be seen that trial signal captures the first arrivals and amplitudes of the fundamental Lamb modes, demonstrating the effectiveness of the automated amplitude ratio extraction.

To visualize the results as a whole, the extracted amplitude ratios $R^\star$ for each source depth may be seen in Fig. 12. For verification, the results are overlain with predictions from the FEM model at 1.5 MHz-mm (i.e. 470 kHz in the 3.18 mm plate). The data points shown for the extracted ratios are an average of the 32 simulations at each source depth, with two standard deviations shown as vertical error bars. It should be noted that the width of the pencil lead (0.5 mm) was not entirely negligible with respect to the plate thickness. This width is therefore shown as horizontal error bars in Fig. 12, in order to visualize the uncertainty in the tested depth. The results in Fig. 12 closely match the FEM predictions, demonstrating that the PLBs well approximate edge point forces, and suggesting the potential for depth characterization. If there is any systematic error, it appears that there is a slight underestimation of the measured amplitude ratio. This may be due to the fact that if there is any small vertical component in a PLB, it will disproportionately favor $A_0$, thus artificially increasing the measured amplitude ratio. Inspecting the vertical error bars, it may be noted that the uncertainty of the amplitude ratio increased monotonically from mid-plane to top-plane. This may be explained by considering that the measurement uncertainty for amplitude ratio will increase when the amplitudes become more different (i.e. as the source approaches the top-plane).

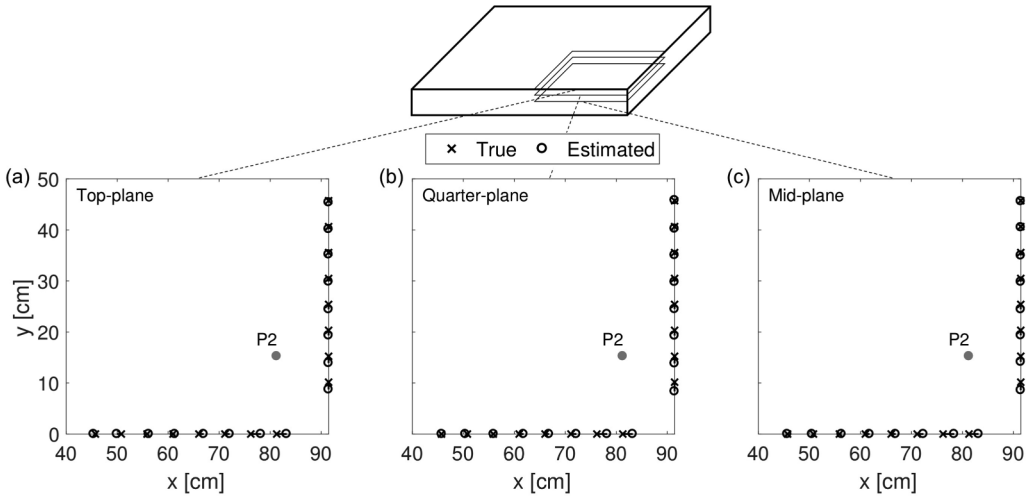


**Fig. 10.** Aluminum plate: Planar localization results overlain with true locations for acoustic emission sources along the (a) top-plane $z' = h$, (b) quarter-plane $z' = h/2$, and (c) mid-plane $z' = 0$. Note: only lower right quadrant of plate shown.

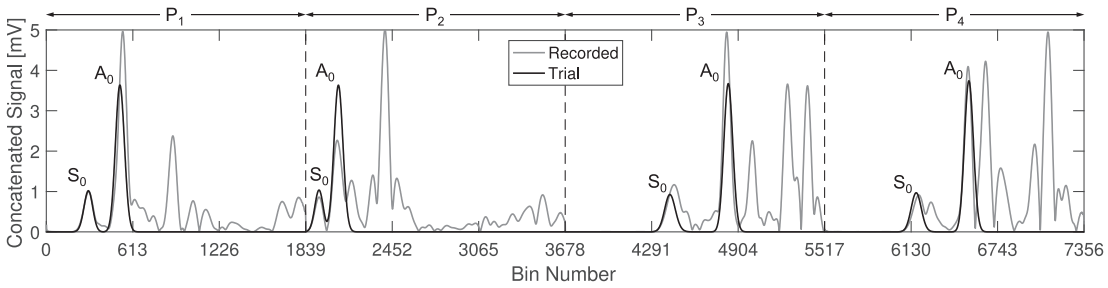


**Fig. 11.** Aluminum plate: Comparison of recorded signal envelopes (after filtering) and trial signal envelopes, showing extraction of first arrivals for $S_0$ and $A_0$ modes. Signals for each sensor $P_1$,…,$P_4$ indicated..

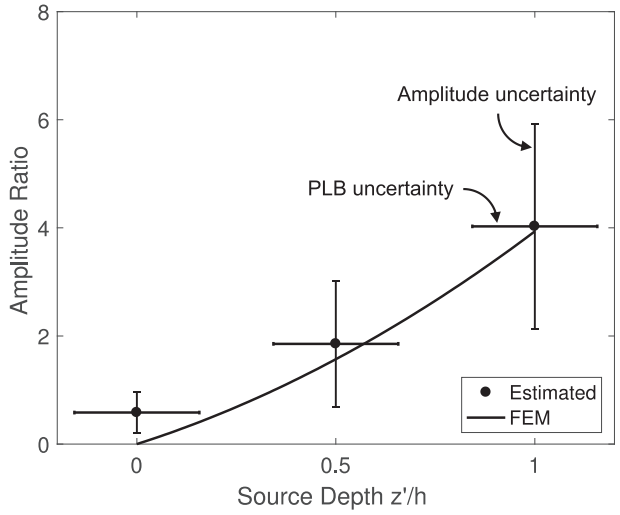


**Fig. 12.** Aluminum plate: Average amplitude ratios and associated uncertainty for top-, quarter-, and mid-plane acoustic emission. Width of pencil lead break (0.5 mm) indicated by horizontal error bars.

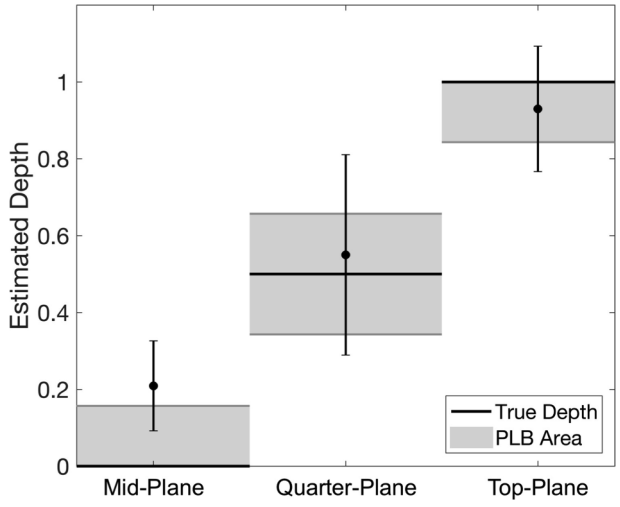


**Fig. 13.** Aluminum plate: Source depth estimation $z^\star/h$ for each depth plane shown over a half-thickness of the plate, with pencil lead break areas shaded. Error bars represent 95% confidence interval.

Source depth estimation using the extracted amplitude ratios may be seen in Fig. 13. In particular, the FEM prediction was used to perform the conversion from amplitude ratio $R^\star$ to source depth $z^\star$ using Eq. 14. For an effective sensor size of 3.75 mm, the fitted parameters in the equation at 1.5 MHz-mm were found to be $p = 2.42$ and $q = 1.64$, with the resulting polynomial function shown in Fig. 12. The results in Fig. 13 are overlain with the true source depth, represented by a dashed line within the shaded PLB area. The PLB area is then used to represent the uncertainty in the true depth. Good agreement is shown between the true source depth and that estimated using the inversion algorithm. As in Fig. 12, the uncertainty increased from mid- to quarter-plane. However, the uncertainty in the top-plane was relatively less, due to the fact that source depths estimated beyond $z^\star/h = 1$ were set to 1. The overestimation of source depth noted previously (potentially due to systematic experimental error) may also be seen here in the mid- and quarter-plane cases. For the top-plane, however, the depth is underestimated since no estimations will exceed the plate thickness. Lastly, it may be noted that the computation time required for the entire inversion algorithm was 0.8 s on average, demonstrating the potential for real-time monitoring.

### 5.2. Fuselage panel

Planar localization results for each of the tested source depths in the fuselage panel are shown in Fig. 14. As in Section 5.1, the triangulation technique was performed with all four sensors, and therefore included some wave paths passing through the riveted stringers (see Fig. 9). However, the good agreement between the true and estimated locations verifies that the $S_0$ velocity was not detrimentally affected by the rivets and stringer. As with localization for the aluminum plate, the estimated source locations were nearly identical between the tested source depths. The average error among all simulated sources was 1.2 cm, with the largest error being 3 cm (slightly larger than for the aluminum plate).

The amplitude ratio was extracted in an analogous manner to the aluminum plate study, and the source depth was estimated as shown in Fig. 15. Although the $S_0$ velocity was not significantly affected by the riveted stringer, it is possible that the amplitudes of the two fundamental modes may be affected to different extents. Therefore, only those sensors which were not separated from the source by a stringer (i.e. $P_1$ and $P_2$) were used to perform depth estimation. To convert the amplitude ratio to source depth $z^\star$, the parameters in Eq. (14) were found to be $p = 2.44$ and $q = 0.699$. These were derived from the FEM

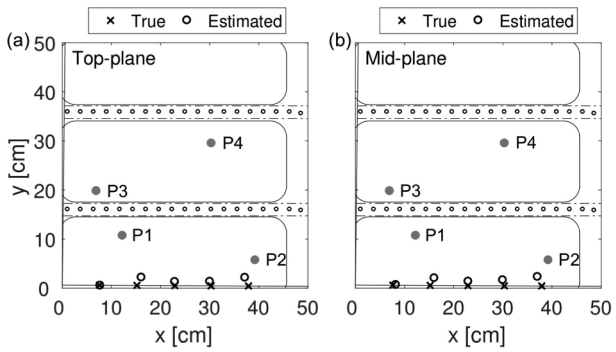


**Fig. 14.** Fuselage panel: Planar localization results for simulated acoustic emission along the (a) top-plane $z' = h$, and (b) mid-plane $z' = 0$.

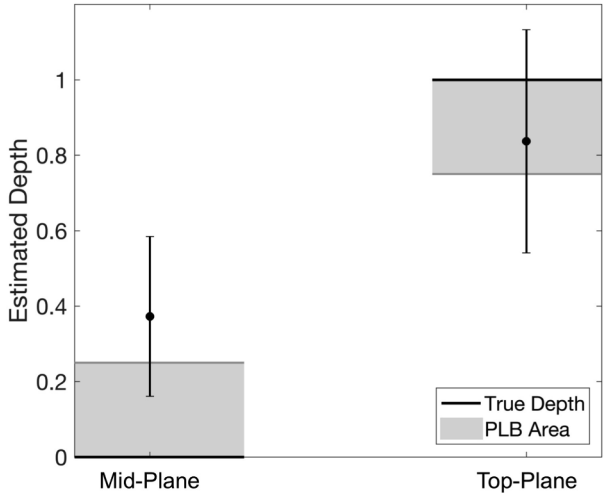


**Fig. 15.** Fuselage panel: Source depth estimation $z^\star/h$ for each simulation plane, with pencil lead break areas shaded. Error bars represent 95% confidence interval.

prediction with $b = 3.75$ mm at 0.94 MHz-mm (i.e. 470 kHz in 2.0 mm plate). It may be seen that the estimated depths show comparably good agreement in accuracy and uncertainty between the mid- and top-plane cases. Considering Fig. 13, the error and uncertainty in both cases were comparable to that found previously. The fact that good agreement was achieved with only two sensors highlights the potential for gathering rich source information in realistic structures with a relatively low-density sensor network. Similar to the aluminum plate study, the required computation time was 0.7 s, further demonstrating the algorithm's real-time monitoring potential.

## 6. Conclusions

This paper proposed an inversion algorithm (AEDep) for the estimation of AE source depth in plate-like structural components. The algorithm was tested on an aluminum plate and a fuselage panel from a Boeing 777 aircraft, in order to evaluate ideal and realistic components, respectively. The algorithm was validated for characterizing controlled horizontal edge forces, obtained via Hsu-Nielsen pencil lead breaks.

Good agreement was found between the true depths of AE sources in the aluminum plate and those estimated using the proposed algorithm. The fact that good agreement was found for sources originating outside the convex hull of the sensors demonstrates its versatility for various source locations. Good performance for such locations will be required if the algorithm is applied in the field, where important events like fatigue cracks emanating from rivet holes may be present. However, the fact that different source depths were also able to be distinguished in the fuselage shows promise for implementing the algorithm in realistic plate-like structures. From the observed uncertainties, the algorithm has the potential to distinguish sources near the surfaces and the mid-plane in such thin plate-like structures (roughly 2 mm thick). Since there was some overlap in the uncertainties between surface and quarter-plane sources, it may prove challenging to achieve resolution on the order of quarter-planes within depth characterization. Along with the fast computation demonstrated in both experimental cases, the results demonstrate the potential to monitor crack growth through the thickness of plate-like structures in real-time. Lastly, due to the symmetry of the amplitude ratio with respect to the thickness of a plate, whether a source originates from the top or bottom half of the thickness cannot strictly be determined.

With the algorithm validated against controlled sources, further research should focus on Lamb waves generated from cracking mechanisms to enable source depth characterization under real cracking scenarios. Future work may also further investigate the effect of the number of sensors used, while potentially determining the minimum number required.

## Acknowledgments

This work was supported by the Office of Naval Research grant #N00014-17-1-2367. The authors would also like to thank The Boeing Company for donating the Boeing 777 fuselage panel used in the experiments.

## Appendix A. Lamb mode amplitudes

The amplitude of a Lamb mode due to a buried force is [25]

$$A = -\frac{\mathrm{i}kVW}{4M} \tag{A.1}$$

where, for symmetric modes, the parameters in the above are defined:

$$\begin{aligned}
V &= a_1\cos(\alpha z') + a_2\cos(\beta z') \\
W &= a_3\sin(\alpha h) + a_4\sin(\beta h) \\
M &= \mu[c_1\cos^2(\alpha h) + c_2\cos^2(\beta h)] \\
a_1 &= 2\cos(\beta h) \\
a_2 &= -\frac{k^2-\beta^2}{k^2}\cos\left(\alpha h\right) \\
a_3 &= -\frac{2\alpha}{k}\cos(\beta h) \\
a_4 &= -\frac{k^2-\beta^2}{\beta k}\cos\left(\alpha h\right) \\
c_1 &= \frac{k^4-\beta^4}{2\beta^3 k^3}[2\beta h(k^2-\beta^2) - (k^2+7\beta^2)\sin(2\beta h)] \\
c_2 &= \frac{k^2+\beta^2}{\alpha k^3}[4\alpha h k^2 + 2(k^2-2\alpha^2)\sin(2\alpha h)]
\end{aligned} \tag{A.2}$$

with the wavenumber-like terms $\alpha$ and $\beta$ defined as $\alpha^2 = \omega^2/V_\mathrm{l}^2 - k^2$, and $\beta^2 = \omega^2/V_\mathrm{t}^2 - k^2$. The bulk wave velocities are defined in terms of the Lamé constants $\lambda$, $\mu$ and density $\rho$ as $\rho V_\mathrm{l}^2 = \lambda + 2\mu$ and $\rho V_\mathrm{t}^2 = \mu$. For antisymmetric modes, the parameters are instead defined:

$$
\begin{aligned}
V &= a_1\sin(\alpha z') + a_2\sin(\beta z') \\
W &= a_3\cos(\alpha h) + a_4\cos(\beta h) \\
M &= \mu[c_1\sin^2(\alpha h) + c_2\sin^2(\beta h)] \\
a_1 &= 2\sin(\beta h) \\
a_2 &= -\frac{k^2-\beta^2}{k^2}\sin\left(\alpha h\right) \\
a_3 &= \frac{2\alpha}{k}\sin(\beta h) \\
a_4 &= \frac{k^2-\beta^2}{\beta k}\sin\left(\alpha h\right) \\
c_1 &= \frac{k^4-\beta^4}{2\beta^3 k^3}[2\beta h(k^2-\beta^2) + (k^2+7\beta^2)\sin(2\beta h)] \\
c_2 &= \frac{k^2+\beta^2}{\alpha k^3}[4\alpha h k^2 - 2(k^2-2\alpha^2)\sin(2\alpha h)]
\end{aligned}
\tag{A.3}
$$

## Appendix B. Triangulation technique

The iterative triangulation technique adopted here is an adapted version of that presented in [33]. The inputs to the iterative technique are the differential arrival times (voluntarily referenced against sensor 1). These are collected in the vector $\mathbf{T} = [T_{12} \cdots T_{1N}]^T$, where $T_{1n} = t_n - t_1$ is the differential arrival time between sensors 1 and $n$, and a superscript $T$ denotes transpose. For convenience, let the signals $s_1, ..., s_N$ be sorted such that the arrival times $t_1, ..., t_N$ are in ascending order; thus, $T_{1N} \geqslant ... \geqslant T_{12} \geqslant 0$. The technique then iteratively updates an initial location estimate $\mathbf{x}^0 = [x^0\ y^0]^T$ in the plane of the plate until some convergence criterion is reached. The update from the $i$ to the $i+1$ estimate is obtained by adding an update term $\Delta\mathbf{x}^i = [\Delta x^i\ \Delta y^i]^T$, scaled by a small rate term $\epsilon$,

$$\mathbf{x}^{i+1} = \mathbf{x}^i + \epsilon\,\Delta\mathbf{x}^i \tag{B.1}$$

The update term is determined from the residual $\mathbf{r}^i = \mathbf{T} - \mathbf{T}^i$ between the measured differential arrival times and those estimated from the current location $\mathbf{x}^i$ (denoted $\mathbf{T}^i$),

$$\Delta\mathbf{x}^i = (\mathbf{G}^i)^+\mathbf{r}^i \tag{B.2}$$

where a superscript $+$ denotes the pseudo-inverse. For $N$ sensors, the matrix $\mathbf{G}^i$ has dimension $(N-1)\times 2$, and is defined as

$$\mathbf{G}^i = \begin{bmatrix} \frac{\partial T_{12}^i}{\partial x^i} & \frac{\partial T_{12}^i}{\partial y^i} \\ \vdots & \vdots \\ \frac{\partial T_{1N}^i}{\partial x^i} & \frac{\partial T_{1N}^i}{\partial y^i} \end{bmatrix} \tag{B.3}$$

where the spatial derivatives are expressed

$$
\begin{aligned}
\frac{\partial T_{1n}^i}{\partial x^i} &= \frac{1}{V_s}\left(\frac{x^i - x_1}{r_1^i} - \frac{x^i - x_n}{r_n^i}\right) \\
\frac{\partial T_{1n}^i}{\partial y^i} &= \frac{1}{V_s}\left(\frac{y^i - y_1}{r_1^i} - \frac{y^i - y_n}{r_n^i}\right)
\end{aligned}
\tag{B.4}
$$

with $V_s$ the $S_0$ group velocity at the given center frequency (determined from dispersion curves), and $r_n^i = \|\mathbf{x}^i - \mathbf{x}_n\|_2$ the distance between the $i$-th estimated location and sensor $n$. Once the given convergence criterion is reached, the superscript $\bigstar$ is used to denote the final estimate of source location as $\mathbf{x}^\bigstar$. For the experiments conducted in this paper, the initial location estimate $\mathbf{x}^0$ for the iterative technique was taken as the center of a specimen, while the rate term $\epsilon$ was set to $1\times10^{-3}$. The iteration was considered to converge when the $\ell_2$-norm of the update term $\Delta\mathbf{x}^i$ was less than 1 mm.

## References


[1] C.R. Farrar, K. Worden, Structural Health Monitoring: A Machine Learning Perspective, first ed., John Wiley & Sons, 2013 doi:https://doi.org/10.1177/1475921708090560.

[2] D. Broek, Elementary Engineering Fracture Mechanics, third ed., Martinus Nijhoff, The Hague, 1982.

[3] P. Paris, F. Erdogan, A critical analysis of crack propagation laws, J. Basic Eng. 85 (4) (1963) 528–533, https://doi.org/10.1115/1.3656900.

[4] J. Schijve, Fatigue of Structures and Materials, second ed., Springer, Amsterdam, 2009.

[5] T. Kundu, S. Das, K.V. Jata, Point of impact prediction in isotropic and anisotropic plates from the acoustic emission data, J. Acoust. Soc. Am. 122 (4) (2007) 2057–2066, https://doi.org/10.1121/1.2775322.

[6] L. de Marchi, A. Marzani, N. Speciale, E. Viola, A passive monitoring technique based on dispersion compensation to locate impacts in plate-like structures, Smart Mater. Struct. 20 (2011), https://doi.org/10.1088/0964-1726/20/3/035021 035021.

[7] A. Ebrahimkhanlou, S. Salamone, A probabilistic framework for single-sensor acoustic emission source localization in thin metallic plates, Smart Mater. Struct. 26 (2017), https://doi.org/10.1016/j.ultras.2017.03.006 095026.

[8] D. Sen, K. Erazo, S. Nagarajaiah, Bayesian estimation of acoustic emissions source in plate structures using particle-based stochastic filtering, Struct. Control Health Monit. 24 (11) (2017) 1–12, https://doi.org/10.1002/stc.2005.

[9] D. Gagar, P. Foote, P. Irving, A novel closure based approach for fatigue crack length estimation using the acoustic emission technique in structural health monitoring applications, Smart Mater. Struct. 23 (10) (2014), https://doi.org/10.1088/0964-1726/23/10/105033 105033.

[10] M.Y. Bhuiyan, J. Bao, B. Poddar, V. Giurgiutiu, Toward identifying crack-length-related resonances in acoustic emission waveforms for structural health monitoring applications, Struct. Health Monit. 17 (3) (2018) 577–585, https://doi.org/10.1177/1475921717707356.

[11] M.Y. Bhuiyan, V. Giurgiutiu, The signatures of acoustic emission waveforms from fatigue crack advancing in thin metallic plates, Smart Mater. Struct. 27 (1) (2018), https://doi.org/10.1088/1361-665X/aa9bc2 015019.

[12] A. Ebrahimkhanlou, B. Dubuc, S. Salamone, A generalizable deep learning framework for localizing and characterizing acoustic emission sources in riveted metallic panels, Mech. Syst. Signal Pr. 130 (2019) 248–272.

[13] T. Sato, M. Takemoto, K. Ono, Effect of fracture dynamics in thin plate on the waveform and radiation pattern of the lamb waves, Jpn. J. Appl. Phys. 38 (1999) 3193–3200.

[14] M.A. Hamstad, On Lamb modes as a function of acoustic emission source rise time, J. Acoust. Emission 28 (2010) 41–58.
[15] M.R. Gorman, W.H. Prosser, AE source orientation by plate wave analysis, J. Acoustic Emission 9 (4) (1991) 283–288.
[16] M. Surgeon, M. Wevers, Modal analysis of acoustic emission signals from CFRP laminates, NDT & E Int. 32 (6) (1999) 311–322, https://doi.org/10.1016/S0963-8695(98)00077-2.
[17] J.P. McCrory, S.K. Al-Jumaili, D. Crivelli, M.R. Pearson, M.J. Eaton, C.A. Featherston, M. Guagliano, K.M. Holford, R. Pullin, Damage classification in carbon fibre composites using acoustic emission: a comparison of three techniques, Compos. Part B 68 (2015) 424–430, https://doi.org/10.1016/j.compositesb.2014.08.046.
[18] F. Dahmene, S. Yaacoubi, M. El Mountassir, N. Bendaoud, C. Langlois, O. Bardoux, On the modal acoustic emission testing of composite structure, Compos. Struct. 140 (2016) 446–452, https://doi.org/10.1016/j.compstruct.2016.01.003.
[19] B. Dubuc, A. Ebrahimkhanlou, S. Salamone, Simultaneous localization and classification of acoustic emission sources in plates using a guided wave-based sparse reconstruction approach, 11th IWSHM, DEStech Publications Inc., 2017, pp. 1779–1786.
[20] N. Facciotto, M. Martinez, E. Troiani, Source identification and classification of acoustic emission signals by a SHAZAM inspired pattern recognition algorithm, 11th IWSHMh, DEStech Publications Inc., 2017, pp. 1212–1219.
[21] S.F. Wirtz, D. Söffker, Application of shape-based similarity measures to classification of acoustic emission waveforms, 11th IWSHM, DEStech Publications Inc., 2017, pp. 1177–1184.
[22] M.F. Haider, V. Giurgiutiu, A Helmholtz potential approach to the analysis of guided wave generation during acoustic emission events, J. Nondestruct. Eval. Diagn. Progn. Eng. Syst. 1 (2) (2018), https://doi.org/10.1115/1.4038116 021002.
[23] M.F. Haider, V. Giurgiutiu, Analysis of axis symmetric circular crested elastic wave generated during crack propagation in a plate: a Helmholtz potential technique, Int. J. Solids Struct. 134 (2018) 130–150, https://doi.org/10.1016/j.ijsolstr.2017.10.035.
[24] J. Miklowitz, The Theory of Elastic Waves and Waveguides, first ed., North-Holland Publishing Co., Amsterdam, 1978 doi:10.1016/B978-0-444-42021-3.50002-1.
[25] J.D. Achenbach, Y. Xu, Wave motion in an isotropic elastic layer generated by a time-harmonic point load of arbitrary direction, J. Acoust. Soc. Am. 106 (1) (1999) 83–90, https://doi.org/10.1121/1.427037.
[26] G.C. McLaskey, S.D. Glaser, Acoustic emission sensor calibration for absolute source measurements, J. Nondestruct. Eval. 31 (2012) 157–168, https://doi.org/10.1007/s10921-012-0131-2.
[27] K.F. Graff, Wave Motion in Elastic Solids, first ed., Oxford University Press, London, 1975.
[28] M. Abramowitz, I.A. Stegun, Handbook of Mathematical Functions, National Bureau of Standards, 1972.
[29] J. Gary, M.A. Hamstad, On the far-field structure of waves generated by a pencil lead break on a thin plate, J. Acoust. Emission 12 (3–4) (1994) 157–170.
[30] I.A. Viktorov, Ralyeigh and Lamb Waves: Physical Theory and Applications, first ed., Plenum Press, New York, 1967.
[31] P.D. Wilcox, Modeling the excitation of Lamb and SH waves by point and line sources, Rev. Quant. NDE 23 (2004) 206–213, https://doi.org/10.1063/1.1711626.
[32] J.R. Asay, A.H. Guenther, Ultrasonic studies of 1060 and 6061–T6 Aluminum, J. Appl. Phys. 38 (10) (1967) 4086–4088, https://doi.org/10.1063/1.1709077.
[33] C.U. Grosse, M. Ohtsu, Acoustic Emission Testing, first ed., Springer, Berlin, 2008.
[34] J. Hensman, R. Mills, S.G. Pierce, K. Worden, M. Eaton, Locating acoustic emission sources in complex structures using Gaussian processes, Mech. Syst. Signal Process. 24 (2010) 211–223, https://doi.org/10.1016/j.ymssp.2009.05.018.
[35] B. Dubuc, A. Ebrahimkhanlou, S. Salamone, Localization of multiple acoustic emission events occurring closely in time in thin-walled pipes using sparse reconstruction, J. Intel. Mater. Syst. Struct. 29 (11) (2018) 2362–2373.
[36] S. Banerjee, A.K. Mal, Acoustic emission waveform simulation in multilayered composites, J. Strain Anal. 40 (1) (2005) 25–32, https://doi.org/10.1243/030932405X7728.
[37] M.G.R. Sause, Inverstigations of pencil-lead breaks as acoustic emission sources, J. Acoust. Emission 29 (2011) 184–196.
[38] M.A. Hamstad, Acoustic emission signals generated by monopole (pencil-lead break) versus dipole sources: finite element modeling and experiments, J. Acoust. Emission 25 (2007) 92–106, https://doi.org/10.4028/www.scientific.net/AMR.13-14.61.